

Gaojin Li^{1,2,3},† and Donald L. Koch³,†

(Received 10 April 2022; revised 12 September 2022; accepted 22 October 2022)

A recent experiment by Wang et al. (Soft Matt., vol. 17, 2021, pp. 2985–2993) shows that a self-propelled compound drop in a surfactant-laden solution can autonomously change its motion from a straight line to a spiraling trajectory, enhancing its capability for chemical detection, catalytic reaction and pollutant removal in a large fluid region. To understand the underlying physics of this peculiar motion, we develop a two-dimensional minimal model to study the swimming dynamics of a compound droplet driven by a self-generated Marangoni stress. We find that, depending on the Péclet number (Pe) and the viscosity and volume ratios of the two compound phases, the drop can swim in a variety of trajectories, including straight lines, circles, zigzag curves and chaotic trajectories. The drop moves in circles when its two components have comparable volumes. Otherwise, it shows other types of motions depending on Pe. Our simulation results for the circular motion at small Pe are qualitatively comparable to the experiment. The transition between zigzag and circular trajectories is mainly determined by the orientation of high-order modes with respect to the drop's swimming direction. For most compound drops, the speed decays as $Pe^{-1/3}$ at high Péclet numbers as it does for a single-phase drop. A drop with two equal components undergoes a run-and-reorient motion due to the competition between the even and odd modes.

Key words: Marangoni convection, drops

1. Introduction

Over the past decades, self-propulsion of small active drops and particles has been widely studied to understand microorganism locomotion, active matter and non-equilibrium

† Email addresses for correspondence: gaojinli@sjtu.edu.cn, dlk15@cornell.edu

© The Author(s), 2022. Published by Cambridge University Press. This is an Open Access article, distributed under the terms of the Creative Commons Attribution licence (http://creativecommons.org/licenses/by/4.0), which permits unrestricted re-use, distribution and reproduction, provided the original article is properly cited.

¹State Key Laboratory of Ocean Engineering, Shanghai 200240, PR China

²School of Naval Architecture, Ocean and Civil Engineering, Shanghai Jiao Tong University, Shanghai 200240, PR China

³Robert Frederick Smith School of Chemical and Biomolecular Engineering, Cornell University, Ithaca, NY 14853, USA

systems (Herminghaus et al. 2014; Bechinger et al. 2016; Ebbens 2016). Various nano- to micro-sized active drops and particles have been synthesized to perform different tasks in bio-medical and industrial technologies, such as targeted drug delivery (Gao et al. 2015; Singh et al. 2017), bottom-up manufacturing of new materials and structures (Mallory, Valeriani & Cacciuto 2018), and clean-up of oil spills and pollutants for environmental remediation (Gao et al. 2013; Soler et al. 2013; Li et al. 2014). In these applications, compound drops with one phase with special biochemical properties encapsulated in another fluid phase are of increasing interest due to their multifunctionality (Hu et al. 2012; Walther & Muller 2013; Nisisako 2016; Zhang, Grzybowski & Granick 2017). In practice, partially engulfed compound drops are usually unavoidable in production, and more importantly, their configuration is vital in releasing the internal ingredients. Compound droplets made of two partially engulfed immiscible components are also frequently encountered in double emulsification, microfluidic dripping of two streams and fabrication of Janus particles. Previous studies have mainly focused on their static configurations and hydrodynamic responses to an external flow field. In this work the hydrodynamics of the self-propulsion of an active compound droplet will be studied.

The ability of active drops to navigate through a viscous fluid is crucial for directed cargo delivery. The swimming dynamics of an individual drop also determines the hydrodynamic interaction and collective behaviour of multiple drops (Marchetti et al. 2013; Elgeti, Winkler & Gompper 2015). The swimming motion of active drops can be achieved by two mechanisms, diffusiophoresis and Marangoni effects. Both mechanisms are characterized by a mobility factor related to drop size, viscosity and the chemical properties of the drop (Izri et al. 2014; Morozov & Michelin 2019a). The diffusiophoresis motion of the drop is caused by the interaction between the solute species and a short-range potential at the drop interface that generates a slip flow (Anderson 1989; Michelin & Lauga 2014). The Marangoni effect, on the other hand, relies on a gradient of surface tension on the drop interface to drive the motion (Herminghaus et al. 2014; Ryazantsev et al. 2017). The concentration gradient around the drop can be either externally applied (Barton & Subramanian 1989; Brochard 1989), or self-generated through a symmetry-breaking mechanism caused by chemical reaction (Toyota et al. 2009; Thutupalli, Seemann & Herminghaus 2011) or solubilization (Izri et al. 2014; Krüger et al. 2016). More details about this topic can be found in recent reviews (Maass et al. 2016; Ryazantsev et al. 2017). In this work we consider the autonomous motion of a drop driven by a self-generated surface tension gradient. The qualitative results, however, lend insights into active drops utilizing other swimming mechanisms.

The swimming mechanism of an isotropic oil droplet due to the exchange of surfactants between the drop interface and a surrounding micellar solution has been discussed by Herminghaus *et al.* (2014). They showed that the self-propulsion of the drop is caused by the 'molecular pathway' of drop oil diffusing away from the interface. The dissolved oil molecules fill the surfactant micelles in the solution and create a thin boundary layer of depleted free surfactant. At the front of the drop, convection decreases the boundary layer thickness and increases the local surfactant concentration, thereby generating a backward surface tension gradient that propels the drop motion. This process involves the coupled transport and reaction of multiple components, including oil molecules, empty and filled micelles, free surfactant in solution and absorbed surfactant on the drop interface. The critical step for self-propulsion is that the drop creates a positive gradient of surfactant concentration away the interface, which under an incoming flow, increases the surfactant concentration on the interface. For simplicity, in this study we only consider the transport of the surfactant in the bulk fluid with a specified positive normal gradient at the surface. A similar model has also been applied in previous studies of phoretic particles (Michelin,

Lauga & Bartolo 2013; Hu *et al.* 2019) and drops with Marangoni propulsion (Yoshinaga *et al.* 2012; Schmitt & Stark 2013; Yoshinaga 2014; Li 2022).

The self-propelled motion of a single-phase active drop is primarily controlled by the Péclet number $Pe = U_0 a/D$ (Anderson 1989; Michelin *et al.* 2013). This dimensionless number characterizes the ratio between the convective transport of surfactant due to drop mobility and its diffusion, where U_0 is a characteristic fluid velocity driven by surface tension gradients, a is the drop size and D is the surfactant diffusivity. Due to the interaction between drop motion and surfactant transport, even a single-phase, isotropic drop can exhibit complex swimming dynamics. Experiments show that, upon increasing Pe, the trajectory can transform from rectilinear to zigzag, and eventually become chaotic (Krüger *et al.* 2016; Suga *et al.* 2018; Hokmabad *et al.* 2021). At high Pe, the onset of high-order modes and interaction between the drop and the concentration field trigger a nonlinear feedback mechanism that complicates the swimming behaviour (Suda *et al.* 2021).

Different numerical models have been considered to understand the self-propelled motion of a drop in a surfactant solution. In most studies, the drop is modelled as a sphere or a cylinder that isotropically consumes the surfactant at its interface. Michelin and coworkers have undertaken numerous studies on the axisymmetric motion of the drop by a method of spherical harmonics expansion. They found that the type of mode that is most unstable is dependent on the relative strength of the Marangoni and phoretic effects as well as the drop's deformability (Morozov & Michelin 2019a). A drop with a strong Marangoni effect undergoes a steady translation due to a dipole mode (source dipole), whereas a drop with a strong phoretic effect only excites a motionless quadrupole mode (stresslet) and generates a steady symmetric extensional flow (Morozov & Michelin 2019a). Similarly, a moderately deformable drop exhibits a dipole mode and a highly deformable drop exhibits a quadrupole mode (Morozov & Michelin 2019c). Based on a two-dimensional (2-D) drop model, Li (2022) showed that the drop swims as a pusher at a relatively low Péclet number, consistent with the result for a three-dimensional (3-D) drop in Morozov & Michelin (2019c). At high Péclet numbers, the drop transforms between pusher- and puller-like swimming and moves in a zigzag trajectory. Nagai et al. (2013) and Suda et al. (2021) developed a different active drop model assuming the motion is induced by a point source of surfactant attached to the front of the drop surface. This model predicts that with increasing Pe, the drop transforms from a puller to a pusher and the translational motion becomes unstable to external disturbances. The opposite trend is most likely caused by the point source assumption. In experiment, the point source of surfactant is realized by attaching a small soap particle to the drop. Both experiment and linear stability analysis show that the drop moves in a circular trajectory due to a combined effect of anisotropic surface activity and a local no-slip condition at the point of the soap particle (Nagai et al. 2013). We will see that a compound drop has a similar trajectory caused by a different mechanism.

Wang *et al.* (2021) observed that compound drops swim in dynamic trajectories that transform between rectilinear and circular motions. The droplets are made of a mixture of FB oil (hexafluorobenzene) and a multicomponent nematic liquid crystal, E7 (a mixture of hydrogenated cyanobiphenyl and terphenyl mesogens). By tuning the concentration ratio of FB and E7, the drop interior can be either single phased or biphasic (Wang *et al.* 2019). When suspended in an aqueous solution of surfactant, the drop continuously dissolves the FB oil into the solution and undergoes an autonomous motion. The drop is initially single phased but it gradually transforms into a compound drop by losing FB. Eventually it transforms back to single phased with only E7. During these phase transformations, the

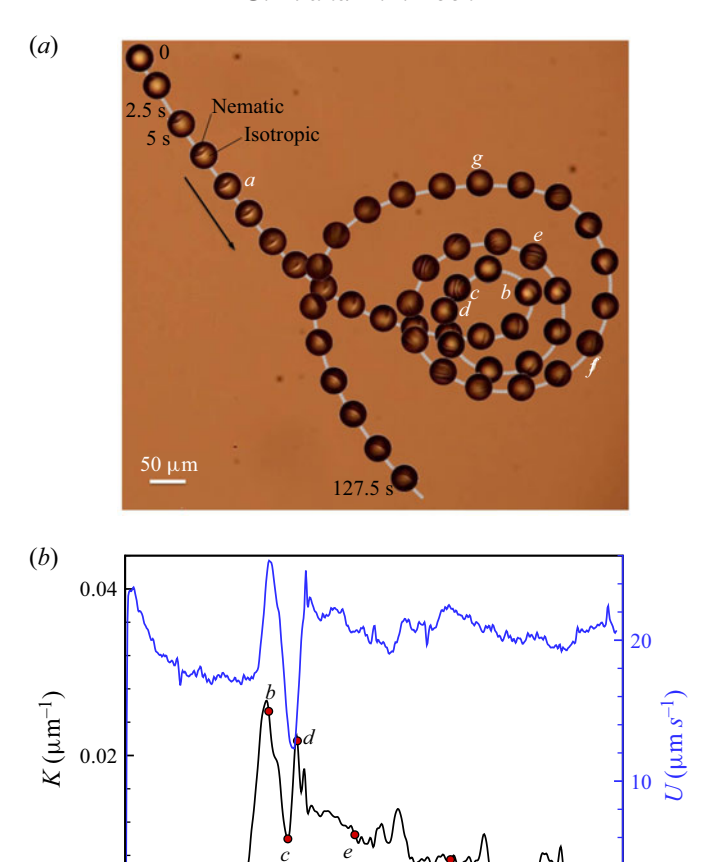


Figure 1. (a) Trajectory of a droplet that transforms between single-phase and compound states in an aqueous solution of surfactant. The droplet is made of a mixture of E7 (a nematic liquid crystal molecule mixture) and FB (an isotropic oil). The dissolution of the FB into the solution generates a propulsive Marangoni stress causing the drop motion whose trajectory changes from a straight line to a circular curve and then returns to a straight line. (b) The corresponding time history of the drop speed and the curvature of the trajectory.

100

50

trajectory of the drop changes from a straight line to a spiralling circle and then back to a straight line again. Figure 1 shows a sequence of images of such a drop moving in a surfactant solution. The curvature of the trajectory rapidly increases after the volume ratio of the nematic and isotropic phases reaches a critical value. The drop speed initially decreases with increasing volume ratio and it exhibits a large oscillation during the early stage of the spiralling motion. This special motion is helpful for the drops to explore a fluid domain for chemical detection, catalytic reaction and pollutant scavenging. Thus, it would be desirable to understand the mechanism for this special trajectory.

Helical and circular trajectories have been observed in previous experiments of single-phase drops of pure nematic liquid crystal (Krüger *et al.* 2016; Suga *et al.* 2018). Suga *et al.* (2018) showed that the helical trajectories occur when the Ericksen number, which is the ratio between the viscous and elastic stresses of the nematic phase, is above a critical value. Morozov & Michelin (2019b) proposed a model to explain the helical motion

by introducing a phoretic velocity directly induced by the nematic vector. In the experiment of Wang *et al.* (2021), however, both the Ericksen number and the direct phoretic effect of the nematic phase are small at a relatively low *Pe*. Therefore, the drop eventually moves in a ballistic motion when it becomes purely nematic. Transition from straight line translation to spinning motion has also been observed for a self-propelled disk driven by Marangoni stresses on a water surface. Vortex shedding behind the disk is found to be the key reason for the destabilization effect (Sur, Masoud & Rothstein 2019). This effect exists only at relatively large Reynolds number and is absent in Wang's experiment. In this work we consider a general model for two-phase drops with different viscosities and neglect the nematic effect. This model is qualitatively comparable to the drops in experiment when the Marangoni effect dominates the phoretic mobility effect caused by the nematic vector. Indeed, we will show that the compound configuration is the key reason for the circular trajectories observed by Wang *et al.* (2021).

In contrast to single-phase drops, the current understanding of the self-propelled motion of compound drops is much more limited. Most previous studies of compound drops have examined their configurations (Torza & Mason 1970; Mori 1978) and hydrodynamics in external flows (see Johnson & Sadhal (1985) for a review). Early investigations of moving compound drops usually considered drops with simple geometries such as a nearly spherical drop partially engulfed by a thin layer of a second phase (Johnson & Sadhal 1983; Sadhal & Johnson 1983) or a completely engulfed compound drop with two concentric spherical interfaces (Rushton & Davies 1983). Shardt, Derksen & Mitra (2014) showed that the rotation of a 2-D Janus drop in a simple shear flow is strongly affected by the presence of the internal interface. Unlike a single-phase drop, the two-phase drop rotates with a time-varying speed. The maximum angular velocity occurs when the internal interface aligns with the extensional axis of the simple shear flow, and the minimum occurs when the interface aligns with the compressional axis. The internal interface induces an anisotropic resistance on the drop and causes motions that are unattainable for single-phase drops, including drop rotation in a streaming flow (Shklyaev et al. 2013) and cross-flow migration in a shear flow (Díaz-Maldonado & Córdova-Figueroa 2015).

Previous numerical studies of the motion of compound drops due to Maragoni stresses have been restricted to axisymmetric thermocapillary motions. Nir and co-workers have studied the thermocapillary axisymmetric translational motion of a partially engulfed drop by solving the streamfunction in toroidal coordinates (Rosenfeld, Lavrenteva & Nir 2008, 2009; Lavrenteva, Rosenfeld & Nir 2011; Rosenfeld *et al.* 2011). The Marangoni stress on the drop surface is caused by an externally applied temperature gradient. It was found that the speed and direction of the drop motion were influenced by many factors, including viscosity, thermal conductivity, the configuration of the compound drop, the volume ratio of the two phases and the dependence of the surface tension on temperature. In this work we study similar effects on the swimming trajectory of an active compound drop in a surfactant solution including configurations in which the internal drop interface is not symmetric about the direction of the drop velocity. The combined effects of Péclet number and the geometry of the compound phases will be discussed in detail.

We propose a minimalistic model of an active compound drop autonomously swimming in a surfactant solution. To simplify the study, a 2-D drop made of two circular sectors, each representing a different phase is considered. This shape reasonably mimics the actual interfaces of the compound drops in the experiment and allows the use of the classic solution for Stokes flow near a corner (Moffatt 1964) to construct the velocity field inside the drop. The concentration and fluid velocity outside the drop are expanded in a Fourier series. Using this simplified model, our study reproduces some key features

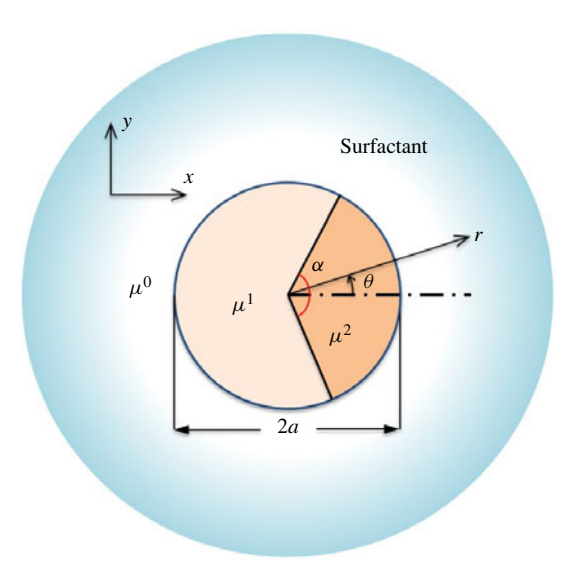


Figure 2. Schematic of a two-phase drop in a surfactant solution. The two regions in the drop are separated by two planar interfaces. The surfactant concentration in the outer fluid decreases with approach toward the drop surface.

that qualitatively match the experimental observations by Wang *et al.* (2021) at small *Pe*. Different swimming behaviours are classified in a parameter space of the Péclet number and the volume and viscosity ratios of the two phases. The rest of this paper is organized as following. Sections 2 and 3 outline the governing equation and mathematical formulation. Section 4 discusses the numerical results of the self-propulsion of the compound drops. The hydrodynamics and transition among different trajectories are studied in detail. Finally, concluding remarks and perspectives are provided in § 5.

2. Governing equations

As shown in figure 2, we consider a 2-D circular oil drop of radius a with phases of viscosity μ^1 and $\mu^2(\geq \mu^1)$ separated by two planar interfaces that meet at an angle α at the drop centre in an outer aqueous solution of viscosity μ^0 . Both internal and external interfaces are assumed to be undeformable. Note that in the experiment, the drop has a curved internal interface and α is unspecified. The angle α is analogous to the volume ratio between the two phases of the drop in the experiment. The current model becomes less realistic at small or large α . The surfactant outside the drop is consumed at the interface at a rate A>0 that is independent of angular position and drop velocity and rotation rate. The surface tension γ^* is assumed to follow a linear relation with the surfactant concentration, $d\gamma^*/dc^*=-\gamma_1$, where c^* is the dimensional concentration and $\gamma_1>0$ is the Marangoni coefficient.

The governing equations are normalized as follows: lengths by a, velocities by $U_0 = AM/D$, time by a/U_0 , pressures and stresses by $\mu^0 U_0/a$, surface tension by $\mu^0 U_0$ and concentration by Aa/D, where D is the surfactant diffusivity in the aqueous solution, $M = a\gamma_1/[2(\mu^0 + \mu^1)]$ is the dimensionless mobility factor describing the strength of the Marangoni effect. It is more convenient to define M and U_0 using μ^1 instead of the mean viscosity $\mu^m = [\mu^1 \alpha + \mu^2 (2\pi - \alpha)]/2\pi$, since μ^m varies with time in the experiment. As will be discussed later, the mean viscosity is more relevant to the average speed of

the drop. In a drop-comoving frame, the governing equations for the incompressible flow and surfactant transport are

$$-\nabla p^j + \beta^j \nabla^2 \mathbf{u}^j = 0, \quad \nabla \cdot \mathbf{u}^j = 0, \quad \text{for } j = 0, 1, 2, \tag{2.1a}$$

$$\frac{\partial c}{\partial t} + \boldsymbol{u}^0 \cdot \nabla c = \frac{1}{P_e} \nabla^2 c, \tag{2.1b}$$

where j=0,1, and 2 represent the aqueous solution and the two regions inside the oil drop, respectively. The pressure p and velocity u must be determined in all three regions, while concentration variation c is only solved in the aqueous solution. The viscosity ratios are $\beta^0=1$ and $\beta^{1,2}=\mu^{1,2}/\mu^0$. The non-dimensional surfactant concentration relative to its far-field value is defined as $c=(c^*-c_\infty^*)/(Aa/D)$, where c_∞^* is the dimensional far-field concentration. The Péclet number $Pe=U_0a/D$ defines the ratio of convection of surfactant to its diffusion. Spontaneous motion of a drop is expected to occur when Pe is above a critical value.

The boundary conditions at the internal and external interfaces are

$$r = 1, \ \frac{\alpha}{2} \le \theta \le 2\pi - \frac{\alpha}{2}: \quad u_r^0 = u_r^1 = 0, \quad u_\theta^0 = u_\theta^1, \quad \tau_{r\theta}^0 - \tau_{r\theta}^1 + \frac{\mathrm{d}\gamma}{\mathrm{d}\theta} = 0, \quad (2.2a)$$

$$r = 1, -\frac{\alpha}{2} \le \theta \le \frac{\alpha}{2}: \quad u_r^0 = u_r^2 = 0, \quad u_\theta^0 = u_\theta^2, \quad \tau_{r\theta}^0 - \tau_{r\theta}^2 + \frac{\mathrm{d}\gamma}{\mathrm{d}\theta} = 0,$$
 (2.2b)

$$\theta = \pm \frac{\alpha}{2}, \ r \le 1: \quad u_{\theta}^1 = u_{\theta}^2 = 0, \quad u_r^1 = u_r^2, \quad \tau_{r\theta}^1 = \tau_{r\theta}^2,$$
 (2.2c)

$$r = 1: \quad \frac{\partial c}{\partial r} = 1. \tag{2.2d}$$

The far-field boundary conditions are

$$r = R: \quad \boldsymbol{u}^0 = -\boldsymbol{U} - \boldsymbol{\Omega} \times \boldsymbol{r},\tag{2.3a}$$

$$r = R: \quad c = 0.$$
 (2.3b)

Since an unbounded 2-D diffusion problem does not have a steady solution at Pe=0, the concentration is assumed to recover c_{∞}^* at a large but finite distance R from the centre of the drop. Equations ((2.2a)-(2.2c)) represent the conditions of zero normal velocity and the continuity of tangential velocity and tangential force at the interfaces; $\tau_{r\theta}^j$ is the $r\theta$ component of the viscous stress tensor $\tau^j=\beta^j(\nabla u+\nabla u^T)$. The force balance at the external interface includes the gradient of surface tension $d\gamma/d\theta=-2(1+\beta^1)\partial c/\partial\theta$. The droplet velocity U and angular velocity Ω are determined by the force- and torque-free conditions,

$$\int_{r=1} \mathbf{n} \cdot \mathbf{\tau}^0 \, \mathrm{d}s = 0, \quad \int_{r=1} \mathbf{r} \times (\mathbf{n} \cdot \mathbf{\tau}^0) \, \mathrm{d}s = 0. \tag{2.4a,b}$$

3. Eigenfunction expansions for velocity and concentration fields

The velocity and concentration fields are solved using a pseudo-spectral method. In two dimensions, the velocity field of an incompressible Stokes flow can be determined from

the streamfunction Ψ as

$$u_r = \frac{1}{r} \frac{\partial \Psi}{\partial \theta}, \quad u_\theta = -\frac{\partial \Psi}{\partial r},$$
 (3.1*a*,*b*)

and the streamfunction satisfies

$$\nabla^2 \nabla^2 \Psi = 0, \tag{3.2}$$

where

$$\nabla^2 = \frac{1}{r} \frac{\partial}{\partial r} \left(r \frac{\partial}{\partial r} \right) + \frac{1}{r^2} \frac{\partial^2}{\partial \theta^2}$$
 (3.3)

and we define θ relative to the centreline of phase 2.

We solve the fluid velocity using an eigenmode expansion as has been done in previous work for a single-phase drop (Nagai *et al.* 2013; Li 2022) and a phoretic solid particle (Hu *et al.* 2019). For a force- and torque-free drop, the streamfunction outside the drop is written as a Fourier series,

$$\Psi^{0} = \frac{\Omega}{2}r^{2} + \text{Re}\left[\sum_{k=1}^{\infty} \frac{r^{2} - 1}{r^{k}} A_{k}^{0} e^{ik\theta}\right],$$
(3.4)

where $\Omega=2\sum_{k=1}Re[A_k^0]\cos(k\alpha/2)$ is the angular velocity of the drop and A_k^0 is the complex coefficient for the kth Fourier mode. The first two modes, k=1 and k=2, correspond to a superposition of a uniform flow and a source dipole and a superposition of a stresslet and a source quadrupole, respectively. In a lab-fixed frame, the x and y velocity components of the drop are

$$U_x = \text{Im}[A_1^0 e^{i\theta_d}], \quad U_y = \text{Re}[A_1^0 e^{i\theta_d}],$$
 (3.5*a*,*b*)

where Re[] and Im[] represent the real and imaginary parts, and $\theta_d(t) = \int_0^t \Omega(t') dt'$ is the orientation angle of the drop in the lab-fixed frame at time t. For a single-phase drop, the streamfunction inside the drop is also written as a Fourier series.

For a two-phase drop, the streamfunction inside the drop is no longer a Fourier series. Its general form is written as

$$\Psi^{j} = \operatorname{Re} \left[\sum_{k=1}^{\infty} r^{\lambda_{k}} \left(A_{k}^{j} e^{i\lambda_{k}\theta} + B_{k}^{j} e^{i(\lambda_{k} - 2)\theta} \right) \right]$$
(3.6)

for j=1 and 2. The eigenvalue λ_k may be a complex number and a non-singular velocity at r=0 requires $\text{Re}[\lambda_k] \geq 1$. Applying the boundary conditions (2.2c) at $\theta=\pm\alpha/2$, λ_k is solved by setting $\text{Det}(\mathbf{A})=0$, where

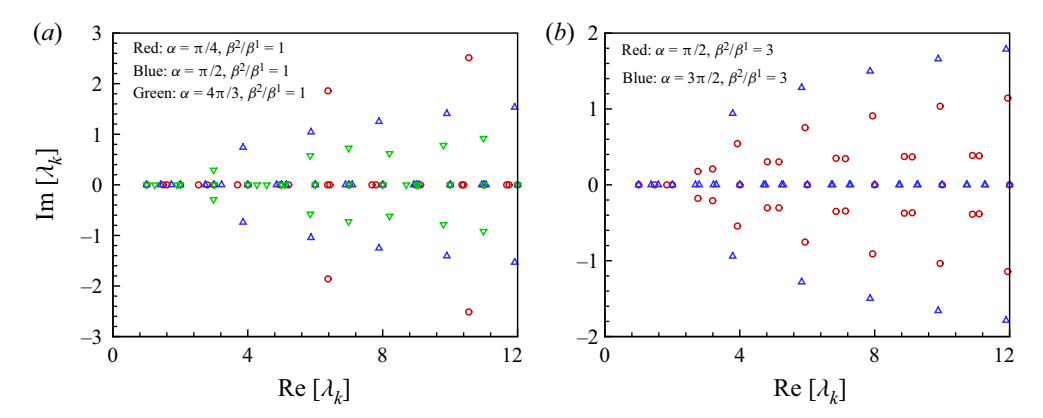


Figure 3. Typical eigenvalue distributions for two-phase drops with different angles α and viscosity ratios β^2/β^1 .

 $\beta = \beta^2/\beta^1$, $\lambda_k' = \lambda_k - 2$, $s_1 = \sin(\lambda_k(\alpha/2))$, $s_1' = \sin(\lambda_k'(\alpha/2))$, $s_2 = \sin[(\lambda_k(2\pi - \alpha/2))]$, and $s_2' = \sin[(\lambda_k'(2\pi - \alpha/2))]$ with similar definitions for c_1 , c_1' , c_2 , c_2' after replacing sine with cosine. The eigenproblem $\mathbf{A} \cdot \mathbf{x} = 0$ is solved to find the coefficients

$$\mathbf{x} = \left(1, \frac{\text{Re}[B_k^1]}{\text{Re}[A_k^1]}, \frac{\text{Im}[B_k^1]}{\text{Re}[A_k^1]}, \frac{\text{Im}[A_k^1]}{\text{Re}[A_k^1]}, \frac{\text{Re}[A_k^2]}{\text{Re}[A_k^1]}, \frac{\text{Re}[B_k^2]}{\text{Re}[A_k^1]}, \frac{\text{Im}[A_k^2]}{\text{Re}[A_k^1]}, \frac{\text{Im}[B_k^2]}{\text{Re}[A_k^1]}\right)^{\text{T}}$$
(3.8)

for the eigenfunctions (3.6) inside the drop. Note that multiple eigenfunctions may exist for the same λ_k . For each eigenfunction, there is one coefficient not given by (3.8) that should be determined by the boundary conditions (2.2a) and (2.2b) at r = 1 (Re[A_k^1] in our simulation). For arbitrary α , numerical calculation of the eigenvalues λ_k is needed. Figure 3 shows some examples of the eigenvalues for drops with different α and $\beta = \beta^2/\beta^1$.

For an evenly divided drop, i.e. $\alpha = \pi$, the eigenfunctions inside the drop can be further simplified. In this case, all the eigenvalues are integers,

$$\lambda_k = 1, 2, 3, \dots, \tag{3.9}$$

and the corresponding streamfunctions are

$$\Psi^{1} = A_{1}r\cos\theta + r^{2}[B_{2}\sin 2\theta + D_{2}\beta(\cos 2\theta + 1)]$$

$$+ \sum_{k=3,5,...} r^{k}\{A_{k}\cos k\theta + (B_{k} - C_{k}k)\cos(k - 2)\theta + D_{k}\beta[\sin k\theta + \sin(k - 2)\theta]\}$$

$$+ \sum_{k=4,6,...} r^{k}\{A_{k}\sin k\theta + (B_{k} - C_{k}k)\sin(k - 2)\theta + D_{k}\beta[\cos k\theta + \cos(k - 2)\theta]\},$$

$$(3.10a)$$

$$\Psi^{2} = A_{1}r\cos\theta + r^{2}[B_{2}\sin 2\theta + D_{2}(\cos 2\theta + 1)]$$

$$\Psi = A_1 r \cos \theta + r \left[B_2 \sin 2\theta + D_2 (\cos 2\theta + 1) \right]
+ \sum_{k=3,5,...} r^k \left\{ \left[A_k + C_k (k-2) \right] \cos k\theta + B_k \cos(k-2)\theta + D_k \left[\sin k\theta + \sin(k-2)\theta \right] \right\}
+ \sum_{k=4,6,...} r^k \left\{ \left[A_k + C_k (k-2) \right] \sin k\theta + B_k \sin(k-2)\theta + D_k \left[\cos k\theta + \cos(k-2)\theta \right] \right\},$$
(3.10b)

for $\pi/2 \le \theta \le \frac{3}{2}\pi$ and $-(\pi/2) \le \theta \le (\pi/2)$, respectively. The coefficients A_k , B_k , C_k , D_k are all real numbers.

The coefficients of the eigenmodes in the streamfunctions are determined by applying the boundary condition on a set of collocation points on the drop surface using the method of least squares. The same method was used to solve the Stokes flow in a 2-D rectangular cavity (Shankar 1993). We truncate the series (3.4) and (3.6) to the Mth and Nth terms, respectively, and define the total square error on K equidistant points θ_k at r=1 as

$$E_T^2 = E_{u_r}^2 + E_{u_\theta}^2 + E_{\tau_{r\theta}}^2, (3.11)$$

where the errors for normal velocity, tangential velocity and tangential stress are, respectively,

$$E_{u_r}^2 = \sum_{k=1}^K \left(\frac{1}{r} \frac{\partial \Psi_N^j}{\partial \theta} \right)_{\theta_k}^2, \tag{3.12a}$$

$$E_{u_{\theta}}^{2} = \sum_{k=1}^{K} \left(\frac{\partial \Psi_{M}^{0}}{\partial r} - \frac{\partial \Psi_{N}^{j}}{\partial r} \right)_{\theta_{k}}^{2}, \tag{3.12b}$$

$$E_{\tau_{r\theta}}^{2} = \sum_{k=1}^{K} \left[\left(\frac{1}{r} \frac{\partial \Psi_{M}^{0}}{\partial r} - \frac{\partial^{2} \Psi_{M}^{0}}{\partial r^{2}} \right) - \beta^{j} \left(\frac{1}{r} \frac{\partial \Psi_{N}^{j}}{\partial r} - \frac{\partial^{2} \Psi_{N}^{j}}{\partial r^{2}} + \frac{1}{r^{2}} \frac{\partial \Psi_{N}^{j}}{\partial \theta^{2}} \right) - \frac{\mathrm{d}\gamma}{\mathrm{d}\theta} \right]_{\theta_{k}}^{2}.$$
(3.12c)

The streamfunctions Ψ_M^0 and Ψ_N^j are the truncated series to the first M and N terms for regions outside and inside the drop with j=1,2 for $\alpha/2 \leq \theta_k \leq 2\pi - \alpha/2$ and $-\alpha/2 \leq \theta_k \leq \alpha/2$, respectively. The total error at the collocation points θ_k is minimized when

$$\frac{\partial E_T^2}{\partial C_m^0} = \frac{\partial E_T^2}{\partial C_n^j} = 0, \tag{3.13}$$

where $C_m^0 = \Omega$, A_1^0 , A_2^0 , ..., A_M^0 and $C_n^j = \text{Im}[A_1^j]$, $\text{Im}[A_2^j]$, $\text{Im}[A_3^j]$, ..., $\text{Im}[A_N^j]$ are the coefficients for the basis streamfunctions, j = 1 and 2. At each time step, we solve the M + N + 1 linear algebraic equations to find C_m^0 and C_n^j . The concentration field is then updated using the fluid velocity.

The concentration field is expanded in the θ direction using a truncated Fourier series as

$$c = \hat{c}_0(r) + \text{Re}\left[\sum_{k=1}^{K-1} \hat{c}_k(r)e^{ik\theta}\right],$$
 (3.14)

where for each mode, $\hat{c}_k(r)$ is solved using a second-order finite difference method with a grid number K in the θ direction equal to the number of terms in the Fourier series. The advection of the concentration is treated in an explicit manner and the diffusion term is solved implicitly. A second-order Runge–Kutta scheme is used to discretize time. The simulation is performed in a circular domain with radius R=200 having a uniform grid in the θ direction and a non-uniform grid in the r direction. The domain size is made large enough so that any further increase in size would have a negligible effect on the nonlinear dynamics of the drop motion. The grid number K is chosen such that a set of grid points lie on the planar interface. In typical simulations, M=N=200 and K=240, the grid

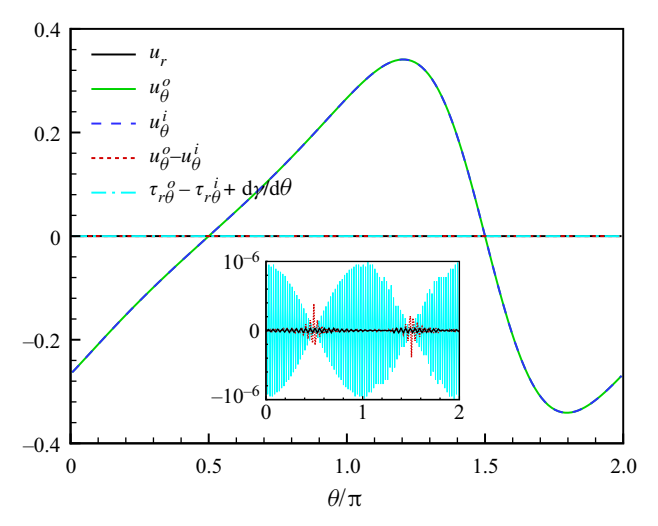


Figure 4. Velocity and force distributions on the external interface of a two-phase drop with $\alpha = \pi$, $\beta^1 = \beta^2 = 1$ and Pe = 6.

number in the r direction is $N_r = 160$ with a constant stretching ratio of approximately 1.03, the finest grid size is $\Delta r_{min} = 0.05$, and the time step is $\Delta t = 0.1$. The computation grids are fine enough to resolve the surfactant boundary layer of thickness $\delta \sim Pe^{1/3} \sim 0.3$ at Pe = 50, the highest Péclet number in this work. The results are confirmed to be well convergent when compared with computations using finer spatial and temporal resolutions. To illustrate that the boundary conditions are well satisfied at the external interface of the drop, figure 4 shows the velocity and stress distribution at r = 1 for a drop with $\alpha = \pi$, $\beta^1 = \beta^2 = 1$ and Pe = 6. For the velocity and force continuity conditions, the errors are less than 10^{-6} . The maximum error for velocity occurs at the two internal interfaces.

We also solve the velocity field inside the drop using a finite volume method on a staggered grid to further verify our results. Comparison of the finite volume and spectral solutions indicates that the two results agree well, as shown in figure 14(b) for the time history of speed and angular velocity for a drop of $\alpha = \pi$, $\beta^1 = \beta^2 = 1$ and Pe = 15.

4. Self-propulsion of an active drop

4.1. Single-phase drop

A detailed consideration of the swimming dynamics of a 2-D single-phase drop can be found in Li (2022). Here, we briefly summarize the main results for comparison with the two-phase drop dynamics. The single-phase drop has no rotation and its self-propelled motion is similar to a 2-D active diffusiophoretic solid particle (Hu *et al.* 2019). The linear stability of a motionless drop shows that the critical Péclet number for the onset of the *k*th mode is

$$Pe_{c,k} = \frac{4k(k-1)(1+R^{2k})}{2k^2 \ln R - 2k \ln R + R^{2k} - k^2 R^2 + k^2 - 1},$$
(4.1)

which is independent of the viscosity ratio $\beta^1 = \mu^1/\mu^0$. As $R \to \infty$, the critical Péclet numbers are $Pe_{c,1} \to 0$ and $Pe_{c,k} = 4k(k-1)$ for $k \ge 2$. Thus, a 2-D drop undergoes spontaneous steady translational motion in an infinitely large fluid domain. We will see that this result also holds for a compound 2-D drop.

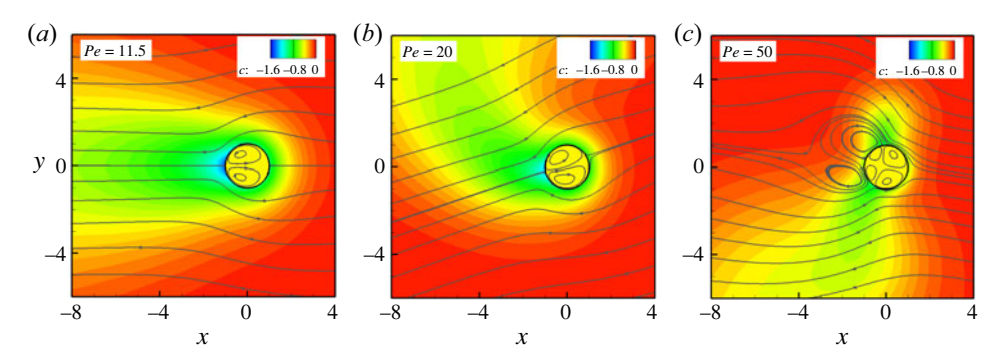


Figure 5. Streamlines and surfactant concentration field near a single-phase drop at different Péclet numbers.

Typical flow fields around a single-phase drop at different Péclet numbers are shown in figure 5. For $Pe \lesssim 11.8$, the drop moves in a straight line at a constant speed, forming two symmetric vortices in its interior and inducing a steady wake with less surfactant. The contraction of the streamlines passing around the drop indicates a pusher-type swimming motion. At higher Pe, the drop moves in a meandering trajectory with square and/or triangle waves and the fluid velocity varies in time between pusher-type and puller-type fields (Li 2022). On a large length scale, the meandering trajectory may form a line, a closed circle or a chaotic pattern. These trajectories are similar to those for an active solid particle (Hu $et\ al.\ 2019$). The single-phase drop has no rotation and the non-ballistic motion is caused by changes in the direction of the translational velocity. The emergence of these complex trajectories is directly related to the asymmetric surface tension distribution on the drop interface, which causes imbalances between the two interior vortices or the emergence of smaller vortices.

Figure 6(a) shows the dependence of the average drop speed $U = \langle U_x^2 + U_y^2 \rangle^{1/2}$ on the Péclet number, where $\langle \rangle$ indicates a time average. The drop motion occurs above approximately Pe = 0.47, which is consistent with linear stability analysis. For $Pe \lesssim 1$, the velocity of the single-phase drop is very close to that for a solid particle. At higher Pe, the drop has a larger speed than a particle. At $Pe \simeq 11.8$, the speed starts to oscillate as the drop undergoes an unsteady meandering motion. Similar to a solid particle, a freely moving drop swims faster than a drop whose motion is restricted to lie on a straight line at the same Pe. In fact, the speed of the restricted translation abruptly decreases to zero at $Pe \geq 14.04$ as the dipole mode (k = 1) is fully suppressed and the drop generates a pure quadrupole mode (k = 2). As we will see later, the swimming dynamics of a compound drop is also strongly influenced by the interaction and competition between dipole and quadrupole modes. At $Pe \sim 39.2$, the amplitude of the speed oscillation increases abruptly. This corresponds to the transformation of the meandering trajectory from square to triangular waves, which causes a sudden decline of the dominant frequency of the drop speed (figure 6b).

4.2. Compound drop

The internal interfaces within a compound drop lead to different velocity modes inside the drop than those in single-phase drops. This significantly influences the drop motion and surfactant transport. The average speed depends not only on the Péclet number but also the volume ratio and the viscosity of the two internal phases. Figure 6 shows the results for drops with two combinations of viscosity, $\beta^1 = \beta^2 = 1$ and $\beta^1 = 1$, $\beta^2 = 3$

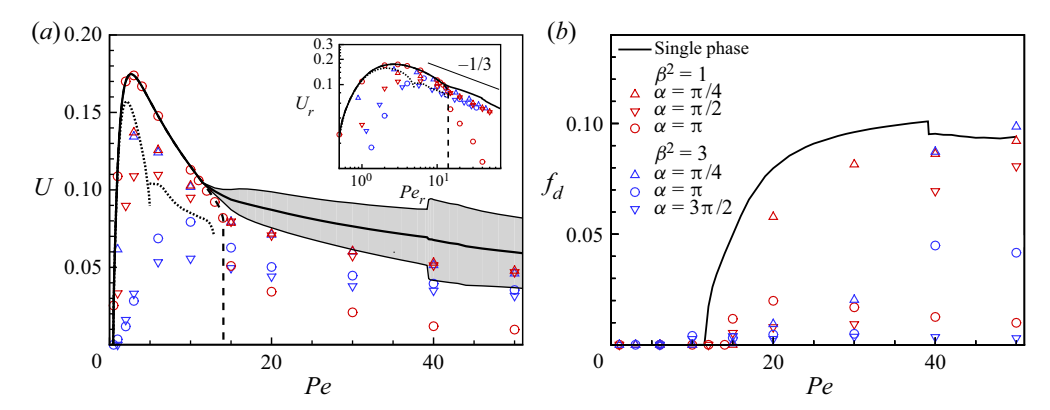


Figure 6. (a) The average speed U of drops at different Péclet numbers. The solid black line shows the speed of a single-phase drop, the shaded area represents the standard deviation of the speed. The dashed line is the speed of a drop when its motion is restricted to follow a straight line. The dotted line is the velocity of an active solid particle (Hu *et al.* 2019). Symbols show the speed of two-phase drops with different combinations of α and β^2 for $\beta^1 = 1$. Inset: the rescaled speed $U_r = \beta_r U$ as a function of the rescaled Péclet number Pe_r (see text for definition). (b) The dominant frequency f_d of the drop speed at different Péclet numbers.

at different interface angles α . Due to the extra flow resistance caused by the internal interfaces, two-phase drops almost always move slower than single-phase drops at the same Pe. The only exception occurs for a drop containing two semicircular phases with the same viscosity. For $Pe \lesssim 14$, this drop moves in a straight line parallel to the planar interface and is unaffected by the interface. At $Pe \gtrsim 15$, the average speed dramatically decreases and the drop moves in a special run-and-reorient motion. The details of this type of drop motion will be discussed later. For the other cases, the two-phase drops show similar trends in drop speed and frequency with increasing Pe as the single-phase drop.

To better compare the speed of different compound drops, we introduce a new characteristic velocity $U_{0r} = U_0/\beta_r$ and Péclet number $Pe_r = U_{0r}a/D = Pe/\beta_r$, where $\beta_r = (\mu^0 + \mu^m)/(\mu^0 + \mu^1)$ and $\mu^m = [\mu^1\alpha + \mu^2(2\pi - \alpha)]/2\pi$ is the mean viscosity. As shown in the inset of figure 6(a), the rescaled data collapses for various combinations of α and β^1 , β^2 and the velocity scales as $U_r = \beta_r U \sim Pe_r^{-1/3}$ for $Pe_r \gtrsim 10$, except for the drops in run-and-reorient motions. The average speed of a compound drop is on average 30% lower than the speed of a single-phase drop. In figure 6(b) the speed for most compound drops has a lower frequency than the frequency of a single-phase drop, indicating different drop motions than the meandering swimming. The compound drop has a non-zero angular velocity, which oscillates at the same frequency as the translational velocity.

Next, we consider the swimming dynamics of compound drops. Figure 7(a) shows typical trajectories for drops with Pe=6, $\beta^1=1$, $\beta^2=3$ and different α . For $\alpha \lesssim \pi$ and $\alpha \gtrsim 1.5\pi$, the drop translates in a rectilinear trajectory, while at intermediate α , its trajectory becomes circular, consistent with the three swimming stages of a compound drop in the experiment. Different from the circular pattern of the zigzag trajectory for a single-phase drop (Li 2022), here the circular trajectory is smooth and can have a small radius. Figure 7(b-f) shows the concentration field and the streamlines near the drops. The regions of low and high viscosity inside the drop are coloured light yellow and orange, respectively. When the drop translates along a straight line, its interior forms pairs of symmetric vortices in each of the circular sectors, and the small vortex pairs are always at the trailing end. When the drop moves in a circular trajectory, the vortices are

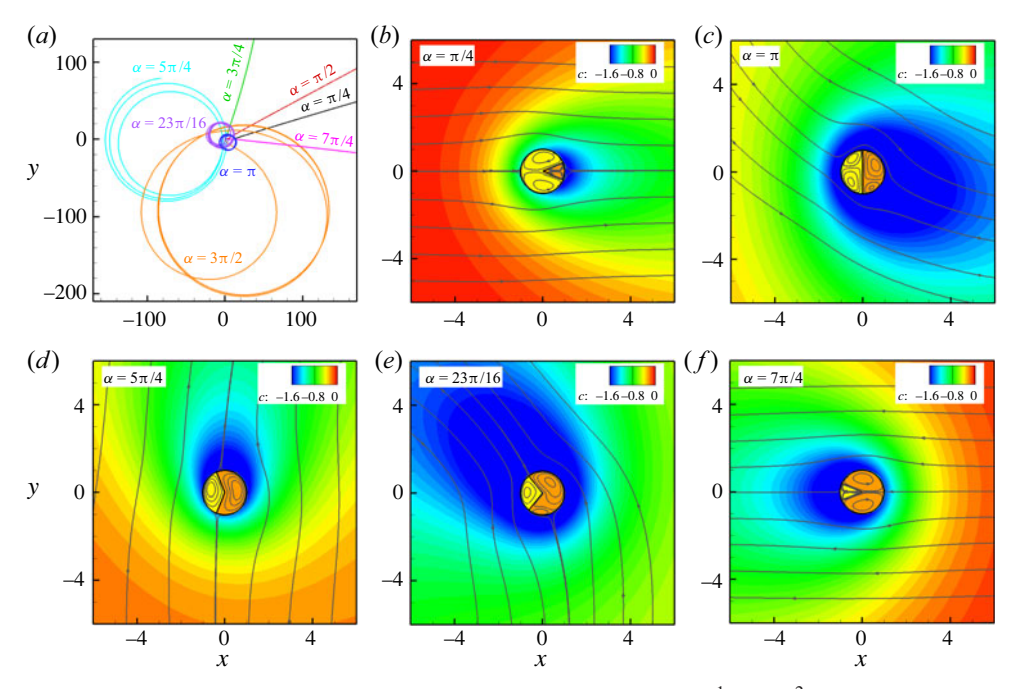


Figure 7. (a) Trajectories of compound drops with different angles α for $\beta^1 = 1$, $\beta^2 = 3$ and Pe = 6. (b-f) Surfactant distribution and streamlines near the compound drops. The low and high viscosity regions inside the drop are represented by the light-yellow and orange colours, respectively.

asymmetric and their arrangement depends on α . The direction of the drop motion can be either roughly normal or parallel to the symmetry axis of the drop. In general, these results qualitatively agree with the experiment, for which the drop motions parallel or perpendicular to the internal interface are both observed. At a large α , the direction of drop motion in simulation is different from the experiment of Wang *et al.* (2021) and the discrepancy is probably related to the sharp corner configuration in our numerical model.

Figure 8 shows the average curvature κ of the trajectory and average speed U for drops with fixed Pe, β^1, β^2 and different interface angles. It mimics the plot for the oil drop with an evolving phase structure in the experiment (see figure 1). Although the 2-D drop model with a static internal drop phase distribution is significantly different from the 3-D drop in the experiment, our simulation does capture some essential features in figure 1(b). For example, the curvature of the trajectory is non-zero only above a critical value of α , above which the curvature has two peaks followed by a gradual decrease. The experiment exhibits a few extra peaks at the late stage of the drop motion. These peaks are related to the drop crossing its own trajectory and cannot be captured by the average curvature in our simulation. The speed of the drop initially decreases with increasing α and then exhibits a large oscillation. Our simulation shows that the speed and curvature are closely correlated with the interior vortices: the speed increases and curvature decreases when the drop has two large interior vortices (figure 7d), and the opposite occurs when the drop forms more vortices with smaller sizes (figure 7c,e). Changing the viscosity inside the drop only quantitatively affects the result. Upon increasing the drop viscosity, the critical angle for the emergence of circular motion increases and the drop speed decreases. In the experiment, the surfactant adsorption rates can be different between the two phases of the drop. To examine this effect, we consider a case with $A^2/A^1 = 0.5$, assuming that

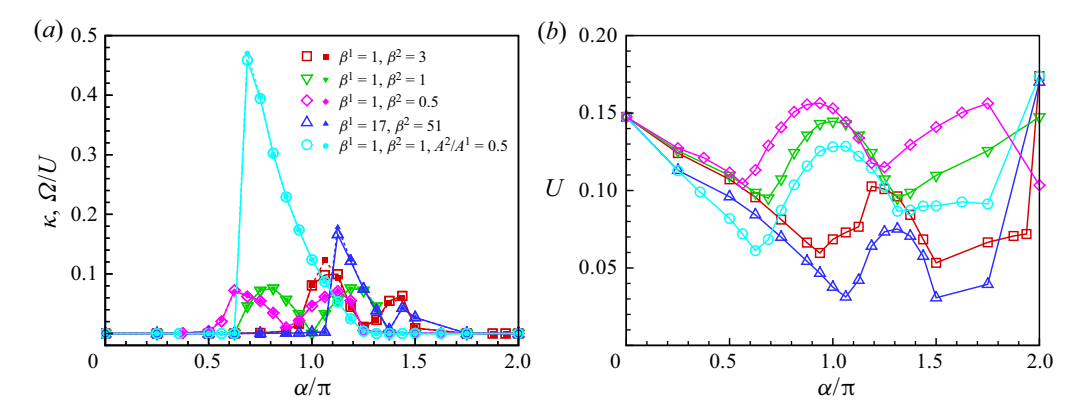


Figure 8. (a) The dependence of the average curvature of the trajectory κ (open symbols and solid lines) and the ratio of average rotation and translation velocities of the drop Ω/U (filled symbols and dotted lines) on the intersect angle α . (b) The dependence of the average speed U on α . The Péclet number of the drop is Pe = 6, $A^2/A^1 = 1$ unless otherwise specified.

the nematic phase (region 2) creates a smaller concentration gradient than the isotropic phase (region 1) due to its lower FB concentration. The curvature of the drop trajectory in this case is single peaked and it has a higher peak value than the cases with uniform adsorption rates. This shows that the additional source of asymmetry promotes the circular motion. We also note that the curvature of the trajectory is close to the ratio of the average rotational and translational velocities of the drop, i.e. $\kappa \simeq \Omega/U$. This means that, for a compound drop, its rigid-body rotation is the main cause for the circular motion.

From the reciprocal theorem, the translational and rotational velocities of a cylindrical swimmer are directly related to integrals of the slip velocity (Elfring 2015)

$$U_{x} = \frac{1}{2\pi} \int_{0}^{2\pi} u_{\theta}|_{r=1} \sin\theta \, d\theta, \quad U_{y} = -\frac{1}{2\pi} \int_{0}^{2\pi} u_{\theta}|_{r=1} \cos\theta \, d\theta, \tag{4.2}$$

$$\Omega = -\frac{1}{2\pi} \int_0^{2\pi} u_\theta|_{r=1} \, \mathrm{d}\theta. \tag{4.3}$$

Therefore, the contributions of small vortices with opposite signs tend to cancel each other and result in a lower speed. The curvature in the simulations is systematically lower than that in the experiment, probably due to the differences in surfactant transport and reciprocal relations for two and three dimensions.

In addition to circular motion, compound drops exhibit a strikingly rich variety swimming dynamics for different combinations of Pe, $\beta^{1,2}$ and α . Figure 9 shows some examples of the drop trajectories found in simulations, including circles, star-shaped circles, quasi-periodic and aperiodic loops, smooth meandering curves, staircase-like zigzag curves and chaotic patterns. These trajectories can be roughly placed into three categories: straight lines, loops and zigzag curves, depending on whether the curvature of the trajectory (or similarly, the angular velocity of the drop) has a preferred sign. Figure 10(a) shows the phase diagram for the three types of trajectories with suggested boundaries for $\beta^1 = 1$, $\beta^2 = 3$. In the diagram, the colour shows the mean value of the absolute curvature and the symbol size indicates the drop speed. The categorization of the star-shaped circular trajectories is less definitive than the others. We designate them as loops since their average curvature is typically large, in contrast to the circular trajectories of a single-phase drop. For a drop with two different phases, the trajectory is a

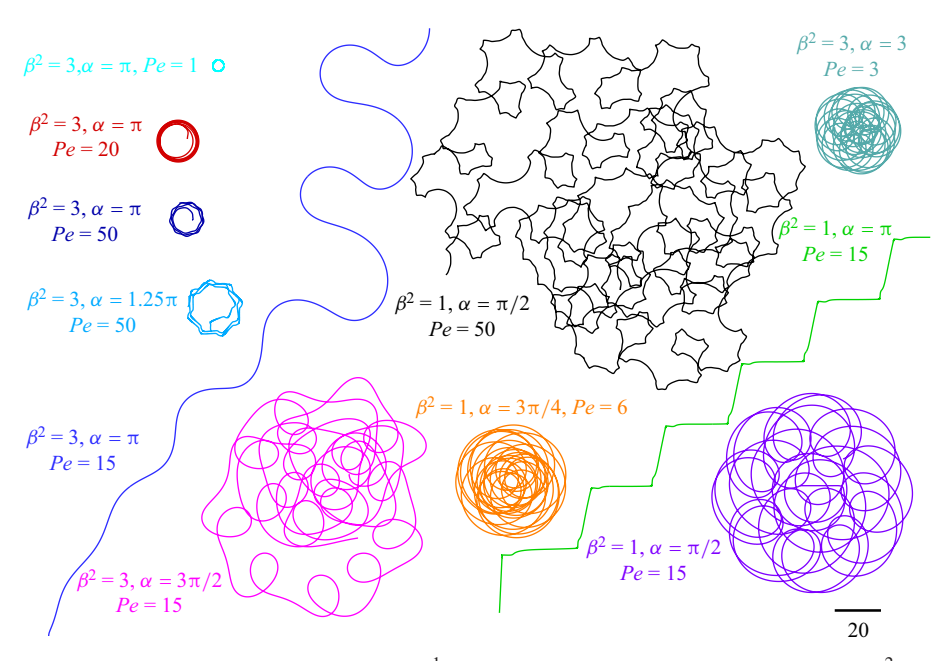


Figure 9. Trajectories of two-phase drops with $\beta^1 = 1$ and different combinations of Pe, α and β^2 . All plots are shown to scale and the scale bar at the bottom right is 20 times the drop size. Animations of the flow fields around the drops are provided in the supplementary movies available at https://doi.org/10.1017/jfm.2022.891.

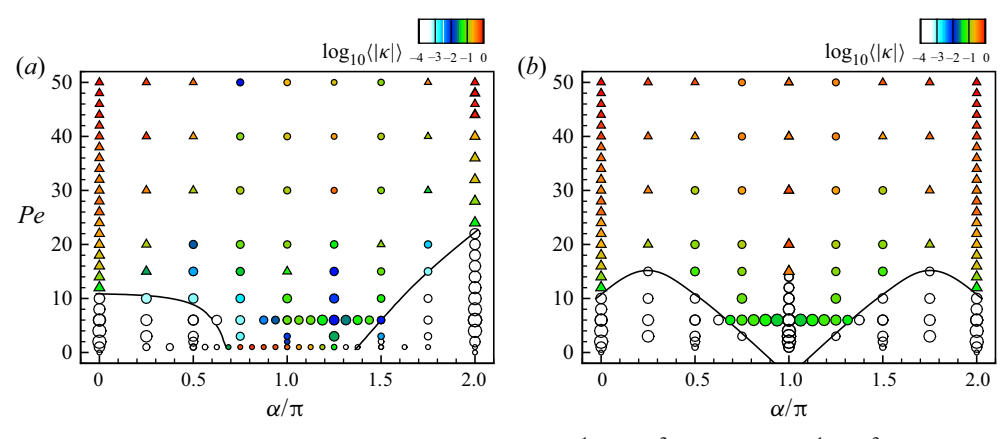


Figure 10. The phase diagram of drop trajectories for (a) $\beta^1 = 1$, $\beta^2 = 3$ and (b) $\beta^1 = \beta^2 = 1$. Triangle symbols represent zigzag trajectories, and circle symbols represent circular and straight trajectories. The lines mark the approximate boundaries between straight line and circular/zigzag trajectories. The colour shows the average absolute curvature of the trajectory. The symbol size represents the average speed of the drop with larger symbols representing larger speeds.

straight/zigzag line at small/large Pe when the drop has a dominant phase ($\alpha \lesssim 0.5\pi$ and $\alpha \lesssim 1.7\pi$), and the trajectory is generally circular when the two phases are comparable in size, although there are a few exceptions. In figure 10(b) a drop having two phases with the same viscosity shows similar behaviour, except at $\alpha = \pi$, when it moves in straight or zigzag lines because of symmetry.

To understand the transition from straight line to circular/zigzag motion, we proposed a reduced model to analyse the linear stability of the translational motion. At the drop's external surface (r = 1), the equation for the surfactant transport is

$$\frac{\partial c}{\partial t} + u_{\theta}^{0} \frac{\partial c}{\partial \theta} = \frac{1}{Pe} \frac{\partial^{2} c}{\partial \theta^{2}} + f(\theta), \tag{4.4}$$

where $f(\theta)$ is the flux of surfactant to the drop surface due to radial diffusion. We only keep the first two modes of the concentration Fourier expansion, $c = \hat{c}_0 + \sum_{k=1}^2 (\hat{c}_k^c \cos k\theta - \hat{c}_k^s \sin k\theta)$, where \hat{c}_k^c and \hat{c}_k^s are the real and imaginary parts of \hat{c}_k in (3.14). We assume the tangential velocity on the drop surface has the same terms as a single-phase drop, $u_\theta^0 = -\Omega + \sum_{k=1}^2 (\hat{c}_k^s \cos k\theta + \hat{c}_k^c \sin k\theta)$ (Nagai *et al.* 2013). This simplified model allows us to consider the drop rotation without knowing the detailed information of $f(\theta)$ or the dynamics of the drop. In the base state, the drop moves along its axis of symmetry and the concentration only has even modes. The non-zero coefficients, \hat{c}_k^c , which determine the drop speed and surfactant distribution, can be directly solved from (4.4), provided that $f(\theta)$, which should also be an even function of θ , is known. Here, however, we will treat \hat{c}_1^c as an adjustable parameter. From the condition of vanishing velocity at $\theta = \pm (\alpha/2)$, we have the angular velocity $\Omega = \hat{c}_1^s \cos(\alpha/2) + \hat{c}_2^s \cos \alpha$, the translational velocity $U_x = \frac{1}{2}\hat{c}_1^c$ and $U_y = -\frac{1}{2}\hat{c}_1^s$, and $\hat{c}_2^c = -\frac{1}{2}\hat{c}_1^c \sec(\alpha/2)$. The perturbation equations for \hat{c}_1^s and \hat{c}_2^s can be written as

$$\frac{\mathrm{d}}{\mathrm{d}t} \begin{pmatrix} \hat{c}_1^s \\ \hat{c}_2^s \end{pmatrix} = \mathbf{A} \cdot \begin{pmatrix} \hat{c}_1^s \\ \hat{c}_2^s \end{pmatrix},\tag{4.5}$$

where

$$\mathbf{A} = \begin{bmatrix} -\frac{1}{Pe} + \left(\cos\frac{\alpha}{2} + \frac{3}{4}\sec\frac{\alpha}{2}\right)\hat{c}_1^c & \left(\frac{3}{2} + \cos\alpha\right)\hat{c}_1^c \\ 2\hat{c}_1^c & -\frac{4}{Pe} + \cos\alpha\sec\frac{\alpha}{2}\hat{c}_1^c \end{bmatrix}. \tag{4.6}$$

Here, we have neglected the perturbations to $f(\theta)$. The non-rotating drop state is stable when both \hat{c}_1^s and \hat{c}_2^s have negative growth rates, i.e. $\operatorname{Det}(\mathbb{A}) > 0$ and $\operatorname{Tr}(\mathbb{A}) < 0$. Otherwise, Ω grows exponentially with time and the straight line motion becomes unstable. Figure 11 shows the stability phase diagram in the space of α and Pe. The parameter \hat{c}_1^c is a function of α and Pe, and its value is estimated to be $|\hat{c}_1^c| \sim 0.1$ –0.4 based on the range of the simulated drop speed. We set \hat{c}_1^c as a negative constant for $\alpha < \pi$, because the drop translates to the negative x direction (figure 7b). For $\alpha > \pi$, positive \hat{c}_1^c should be used since the drop moves in the opposite direction (figure 7f). From (4.6), we can see that the drop rotation is caused by the combined effects of flow stagnation at the interface contact line and the surfactant convection by coupled velocity modes. The analysis predicts that steady translation becomes unstable when α is close to π . The critical Pe for unstable translation decreases as the drop velocity increases. These predictions qualitatively agree with our numerical results.

It might have been thought that the patterns of the drop trajectories could be distinguished by the eigenvalues with circular trajectories occurring when the eigenvalue is imaginary and zigzag trajectories when the eigenvalue is real. However, our results show that the eigenvalues for the two-mode expansion are real for both types of trajectory. As we will see in the following, the higher-order modes ($k \ge 3$) are important for the rotational motion of the drop. This also suggests that the nonlinear interaction between drop swimming and surfactant transport plays a critical role in determining the trajectory of the drop.

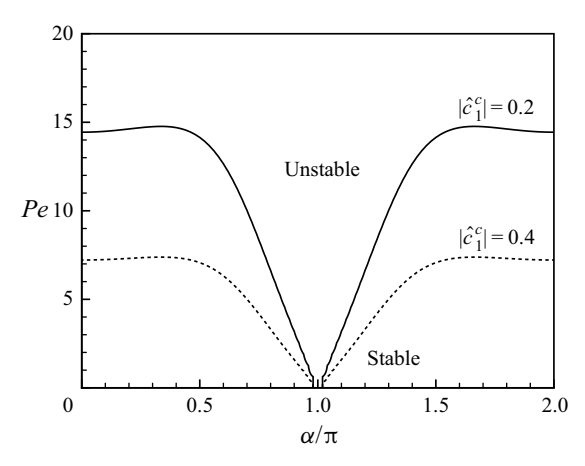


Figure 11. The stability phase diagram on the space of α and Pe predicted by the simplified linear stability model for surfactant transport at the drop interface.

To compare the circular and zigzag motions, figure 12(a) shows the time history of the angular velocity for the drops with $\alpha = \pi$ and $\beta^1 = 3$, $\beta^2 = 3$ at different Péclet numbers. At Pe = 6 and 10, the drop rotates in the counterclockwise direction, and the high viscosity region of the drop is on the inner side of the circular trajectory. At Pe = 20 and 30, the drop reverses its rotation moving in clockwise circles with the high viscosity region on the outer side. At an intermediate Péclet number, Pe = 15, the drop periodically reverses its rotation and moves in a meandering trajectory. In figure 12(b) the distribution of the tangential gradient of surfactant concentration $dc/d\theta$ and tangential velocity u_{θ} on the drop surface look generally similar for all cases. In particular, the lowest concentration (or, equivalently, the largest surface tension), occurs at $\theta \sim 1.6\pi$ in the wake region, creating a flow outward from the interface. The maximum and minimum velocities occur at $\theta \sim 1.3\pi$ and $\theta \sim 1.9\pi$, respectively. The main difference between the fields for drops rotating in different directions appears at $\theta \sim 0.7\pi$, where the drop with counterclockwise rotation has a secondary local peak of $dc/d\theta$ and local minimum of u_{θ} , representing a new vortex inside the drop. Without this vortex, the drop rotates clockwise because the low viscosity region generates a larger slip velocity than the other side (figure 12c,d). At high Péclet number, the drop speed decreases and the induced flow is not strong enough to advect the surfactant downstream to envelope the drop surface. The accumulation of the surfactant at the front of the drop further decreases the local surface tension and creates a strong slip flow that reverses the drop rotation (figure 12f). At the intermediate Pe, transport of surfactant near the front of the drop regularly switches directions and the flow field shifts between the two states. Therefore, the drop periodically changes its rotation direction and moves in a meandering trajectory.

Following Li (2022), we investigate the correlation between the surfactant concentration and the fluid velocity for different drop swimming motions. Figure 13(a) shows the time history of the magnitudes of the flow modes. For each case, the first two modes have the dominant contribution to the drop swimming. At Pe = 20, the stresslet mode (k = 2) has a comparable magnitude as the source dipole mode (k = 1). It generates a strong extensional flow that changes the surfactant distribution around the drop and induces the extra small vortex inside the drop. At Pe = 15, the magnitude ratio between the first modes has a large oscillation.

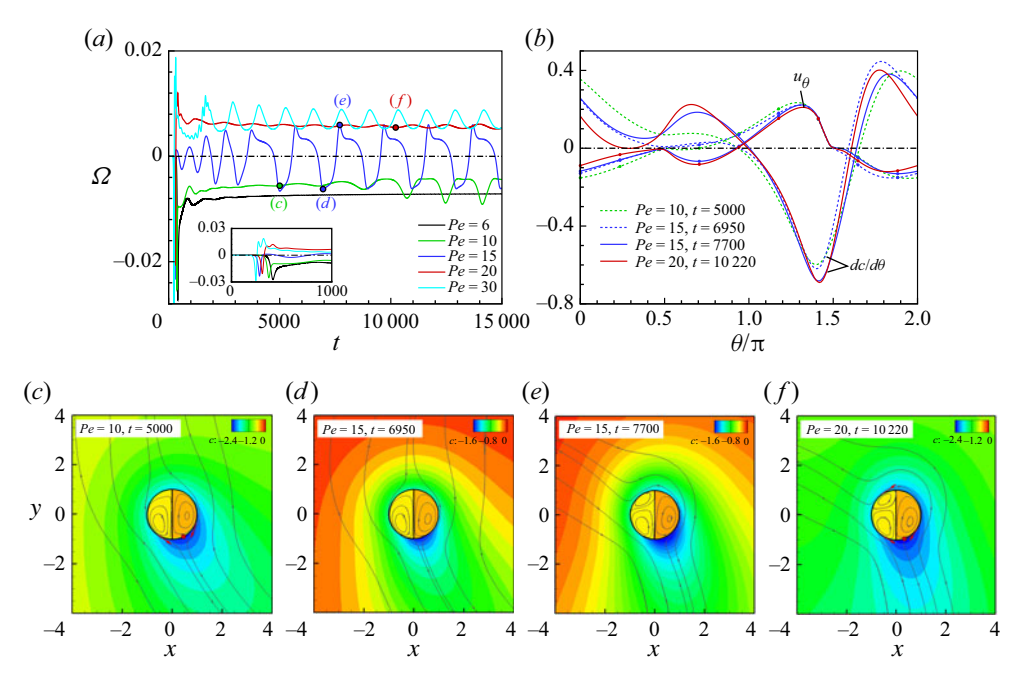


Figure 12. (a) Time history of the angular velocity of drops at different Pe, $\alpha = \pi$, $\beta^1 = 1$ and $\beta^2 = 3$. (b) Distribution of the tangential gradient of surfactant concentration $dc/d\theta$ and tangential velocity u_{θ} on the drop surface. (c-f) Concentration fields and streamlines near the drops. The red point and arrow show the locations of the lowest surfactant concentration and local peaks of tangential velocity on the drop surface.

The orientations of the fluid velocity modes changes with Pe even more than their magnitudes do. Figure 13(b-d) shows the time evolution of the surfactant concentration at the drop surface and the direction of the fluid velocity mode, which for each singularity, is defined by the axis of symmetry of a local converging flow along the drop surface. The results are shown in a drop-fixed frame to reveal the relative angle between the velocity modes and the low concentration wake. The two internal interfaces are located at $\theta = \pi/2$ and $3\pi/2$ in the plots. When the drop moves in a straight line, all velocity modes align with the axis of symmetry of the concentration wake, creating a pusher-type flow field. In comparison, when the drop moves in a non-straight trajectory, the velocity modes do not align in the same direction. For the drop with $\alpha = \pi$, the angular velocity $\Omega =$ $2\sum_{k=1}^{\infty}(-1)^{k-1}Re[A_{2k}]$ is determined by the even modes $(k=2,4,6,\ldots)$. The k=2mode always has a positive angle with respect to the direction of $3\pi/2$ and, therefore, has a negative contribution to the angular velocity. In comparison, the orientation of the k=4mode differs at different Péclet numbers. At Pe = 20, it is on the same side of the internal interface $(3\pi/2)$ as the k=2 mode and causes a positive angular velocity contribution. At Pe = 15, the k = 4 mode oscillates and causes a back-and-forth rotation of the drop and, hence, the zigzag motion.

Finally, we examine the run-and-reorient motion for the special case of a drop with two phases having equal volumes and viscosities, i.e. $\alpha = \pi$, $\beta^1 = \beta^2 = 1$. In figure 14(a) the drop moves in a trajectory composed of piecewise segments with a reorientation angle of approximately 102° . The periodic variation in speed and angular velocity is directly related to the transformations of vortex modes inside the drop. As shown in figure 14(c), the drop forms two vortices inside and swims as a squirmer with an asymmetric slip velocity distribution. The imbalance of the Marangoni stress on the two sides of the drop surface

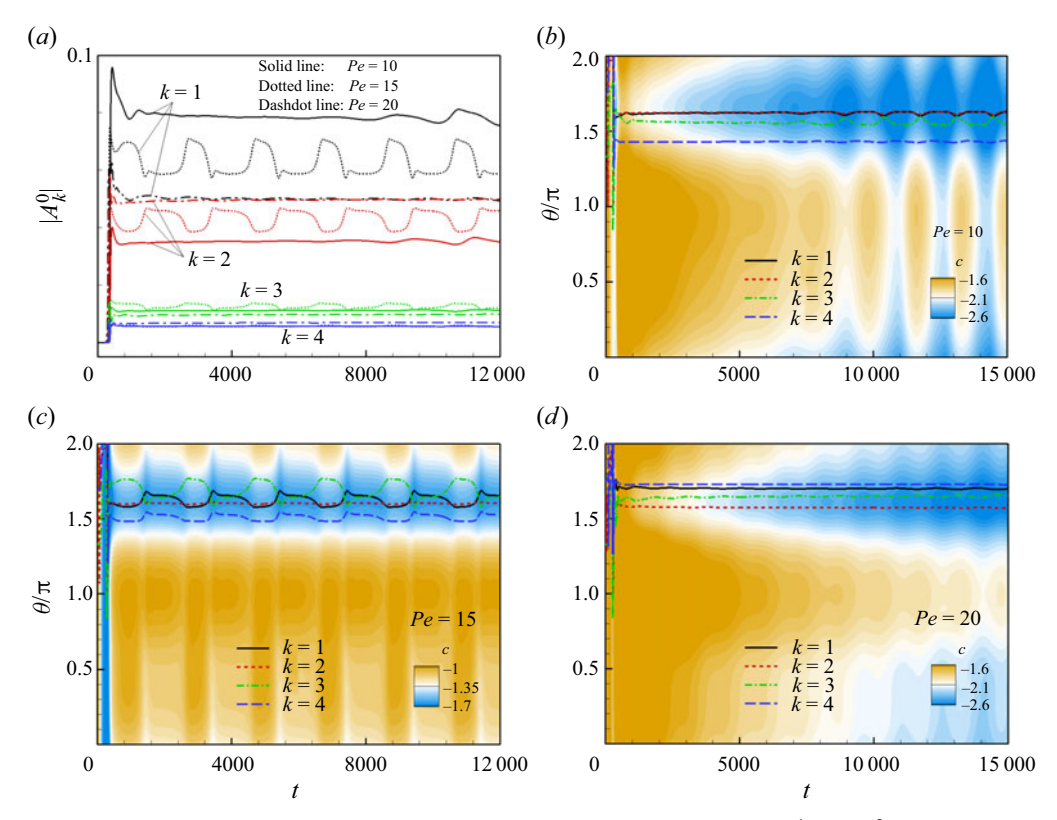


Figure 13. (a) Time history of the magnitude of velocity modes at different Pe, $\beta^1 = 1$, $\beta^2 = 3$ and $\alpha = \pi$. (b-d) The correlation between the surfactant distribution at the drop surface and the orientation of the velocity modes. The results are shown in a drop-fixed frame.

damps the rotation quickly and the drop starts to translate along a straight line with slow rotation ($\Omega \sim 10^{-4}$). This motion is unstable due to the emergence of the quadrupole mode, as occurred for the single-phase drop at $Pe \gtrsim 14$ discussed before, and it generates an extra vortex pair in front of the drop. The extra vortex pair gradually transforms the drop into a pusher-type swimmer and reduces the drop speed (figure 14d). The induced flow causes the surfactant to accumulate at the front stagnation point and creates a surface tension gradient that obstructs the drop motion. Eventually in figure 14(e) the translational motion is largely suppressed and the drop creates a symmetric extensional flow field. This flow is intrinsically unstable due to the attraction between two local maxima of surface tension. Outside the drop, the two regions of low surfactant concentration are advected towards each other and merge at a location that is perpendicular to the internal surface, leading to a fast reorientation and slow translation of the drop. After that, the dipole mode gradually outcompetes the quadrupole mode and the drop repeats the translational motion. The formation of the secondary wake of low concentration in front of the drop is biased along the direction of drop rotation, so that it attracts the main wake and causes the reversal of drop rotation in the next cycle.

Figure 15 shows that the velocity modes for this symmetric drop at Pe = 15 change dramatically during the drop motion. The magnitudes of the odd and even modes are strongly anti-correlated: the odd modes have a large magnitude during the drop's translation stage, while the even modes have a large magnitude when the drop slows down

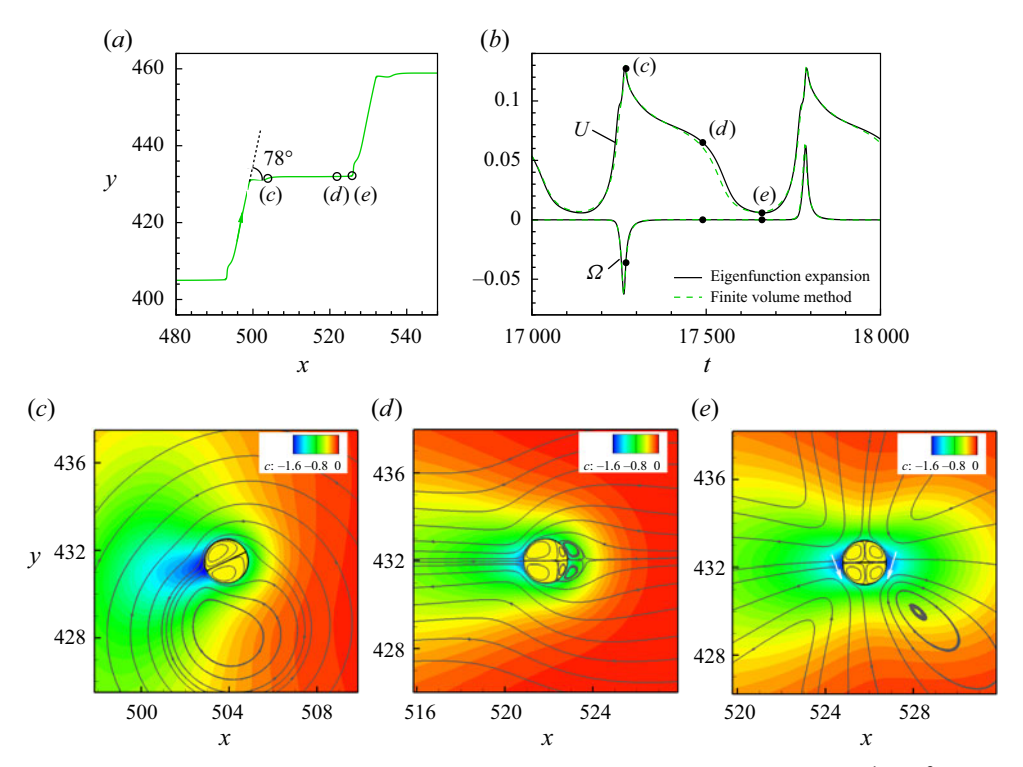


Figure 14. (a) Trajectory of a drop with equal phase volumes and viscosities $\alpha = \pi$, $\beta^1 = \beta^2 = 1$ and Pe = 15. Solid and dashed lines are the results simulated using the eigenfunction expansion and finite volume methods for the interior region of the drop, respectively. (b) Time history of the drop speed and angular velocity. (c-e) Concentration field and streamlines near the drop at the time instants marked in (a,b).

and starts to rotate. In the reorientation stage, the formation of the secondary wake of low surfactant concentration only causes the odd modes to change direction. Meanwhile, the even modes remain aligned with the direction of the main wake until they suddenly change direction causing the sudden rotation of the drop. This type of run-and-reorient motion is similar to the meandering motion of a single-phase drop along a trajectory with triangle waves (Li 2022), but the transition for the two-phase drop is much more abrupt due to the coupling with the drop rotation.

5. Concluding remarks

To summarize, we have investigated the self-propulsion of a 2-D compound drop composed of two circular sectors driven by Marangoni stresses. Compared with a single-phase drop, the internal interface and viscosity difference introduce more complexity in the hydrodynamic flows and cause a variety of swimming trajectories, including straight lines, circles, smooth and staircase-like zigzag curves, as well as chaotic motions. Depending on whether the trajectory has a predominant bending direction, we classify the trajectories into three categories: straight lines, circles and zigzag curves. Generally speaking, the drop moves in a straight line or zigzag curve when one phase is much larger than the other, whereas its trajectory becomes circular when the two phases are of comparable sizes. The direction of the drop rotation is dependent on the Péclet number. At small *Pe*, the drop rotates with its high viscosity region on the inner side, and

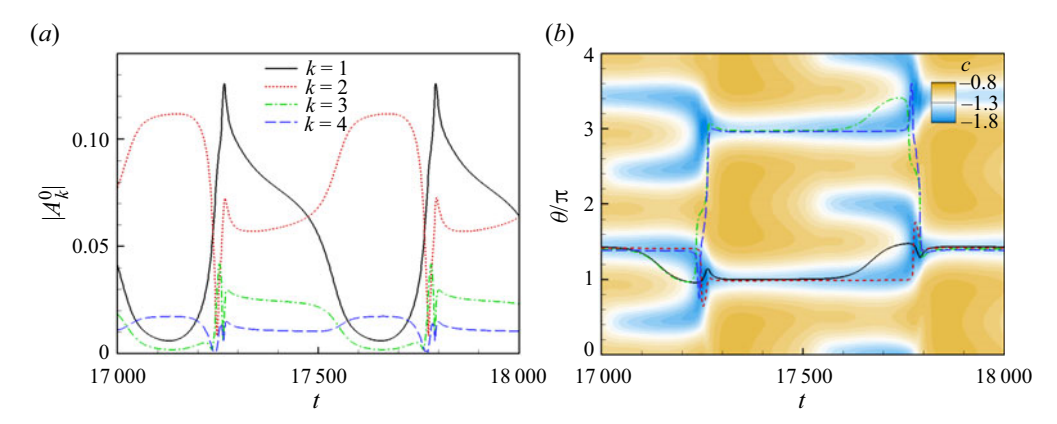


Figure 15. (a) Time history of the magnitude of fluid velocity modes for a drop with Pe = 15, $\alpha = \pi$, $\beta^1 = 1$ and $\beta^2 = 3$. (b) The correlation between the surfactant distribution at the drop surface and the orientation of the flow velocity modes. The results are shown in a lab-fixed frame.

the opposite occurs at high Pe. A difference in viscosity of the two phases inside the drop is not necessary for the circular motion. The average speed, on the other hand, is more sensitive to the Péclet number and average viscosity than the size ratio of the two phases. The presence of the internal interfaces reduces the drop speed. For most of the compound drops, the speed scales as $U \sim Pe^{-1/3}$ for $Pe \gtrsim 10$, which is the same as the scaling for a single-phase drop.

Our numerical results can reproduce the key features of experimental observations of a compound oil droplet with continuous phase transformation (Wang *et al.* 2021). At relatively low Péclet numbers ($Pe \lesssim 10$), our study shows the trajectory transforms from straight lines to smooth circles and eventually back to straight lines with increasing volume ratio of the phases. The curvature of the trajectory has a local minimum when the drop has two large interior vortices rather than multiple small vortices. The drop speed reaches a maximum near the conditions for minimal curvature. These results are consistent with the experiments.

At high Péclet numbers, the drop motion exhibits meandering features due to the onset of instability modes at higher wavenumbers, similar to the motion of a single-phase drop. The numerical simulations also discover a run-and-reorient motion for a drop containing two semicircles of equal viscosity at $Pe \gtrsim 15$. The drop moves along a staircase-like zigzag curve and the flow field inside the drop periodically switches between dipole and quadrupole modes. These results show that the swimming dynamics of the drop is determined by the interplay among various factors: the convection of surfactant around the drop, the distribution of the Marangoni stress on the drop surface, the interior vortices and the difference of flow resistance experienced by the two regions of the drop. The high-order modes play an important role in determining the direction of drop rotation and the pattern of the trajectory.

Several directions can be taken in future research to overcome the limitations of this work. In the current study we use a static drop model to mimic the different stages of a drop with continuous phase transformation. This simplification may partially explain the discrepancies between simulation and experimental results. Transient compositional changes of the drop interior influence the time history of surfactant transport, causing a continuous change in the trajectory curvature in experiment (Wang *et al.* 2021). Future simulations could model the changes to the drop interior as one component of the drop

is transported into the exterior liquid phase. Secondly, current work uses a fixed flux boundary condition for the surfactant while neglecting the potential for the surfactant to be fully depleted near the drop. This assumption is valid if the concentration variation is small and is useful to focus on the basic physics. However, in practice the drop may completely consume the surfactant, particularly when the drop moves in a small circle. As suggested in our simulation (figure 7a), this effect can reduce the curvature of a circular trajectory and cause an outward spiraling trajectory, similar to the experiment. Finally, 3-D simulations of a compound drop are undoubtedly desirable. Other effects, such as the liquid crystal phase and the deformation of the internal interface can also be important. In the inertial regime the trajectory transition due to vortex shedding (Sur *et al.* 2019) can be studied by solving the full Navier–Stokes equations. We also propose that the current simulation may be realized in an experiment using an oil drop floating on the surface of a thin film of surfactant solution (Ichikawa *et al.* 2013; Pimienta & Antoine 2014). The rotation direction of the compound drops can be easily observed to test the simulation results.

Supplementary movies. Supplementary movies are available at https://doi.org/10.1017/jfm.2022.891.

Acknowledgement. We thank X. Wang and N.L. Abbott at Cornell University for insightful discussions and providing experimental data and animation for figure 1.

Funding. G.L. is Funded by the Scientific Research Staring Foundation (grant no. WH220401009). D.L. Koch acknowledges funding from NSF grant no. 2135617.

Declaration of interests. The authors report no conflict of interest.

Author ORCIDs.

- © Gaojin Li https://orcid.org/0000-0001-7694-2430;
- Donald L. Koch https://orcid.org/0000-0002-5474-879X.

REFERENCES

ANDERSON, J.L. 1989 Colloid transport by interfacial forces. Annu. Rev. Fluid Mech. 21 (1), 61–99.

BARTON, K.D. & SUBRAMANIAN, R.S. 1989 The migration of liquid drops in a vertical temperature gradient. J. Colloid Interface Sci. 133 (1), 211–222.

BECHINGER, C., DI LEONARDO, R., LÖWEN, H., REICHHARDT, C., VOLPE, G. & VOLPE, G. 2016 Active particles in complex and crowded environments. *Rev. Mod. Phys.* 88 (4), 045006.

BROCHARD, F. 1989 Motions of droplets on solid surfaces induced by chemical or thermal gradients. *Langmuir* 5 (2), 432–438.

DÍAZ-MALDONADO, M. & CÓRDOVA-FIGUEROA, U.M. 2015 On the anisotropic response of a Janus drop in a shearing viscous fluid. *J. Fluid Mech.* **770**, R2.

EBBENS, S.J. 2016 Active colloids: progress and challenges towards realising autonomous applications. *Curr. Opin. Colloid Interface Sci.* 21, 14–23.

ELFRING, G.J. 2015 A note on the reciprocal theorem for the swimming of simple bodies. *Phys. Fluids* **27** (2), 023101.

ELGETI, J., WINKLER, R.G. & GOMPPER, G. 2015 Physics of microswimmers–single particle motion and collective behavior: a review. *Rep. Prog. Phys.* **78** (5), 056601.

GAO, W., DONG, R., THAMPHIWATANA, S., LI, J., GAO, W., ZHANG, L. & WANG, J. 2015 Artificial micromotors in the mouse's stomach: a step toward in vivo use of synthetic motors. ACS Nano 9 (1), 117–123.

GAO, W., FENG, X., PEI, A., GU, Y., LI, J. & WANG, J. 2013 Seawater-driven magnesium based janus micromotors for environmental remediation. *Nanoscale* 5 (11), 4696–4700.

HERMINGHAUS, S., MAASS, C.C., KRÜGER, C., THUTUPALLI, S., GOEHRING, L. & BAHR, C. 2014 Interfacial mechanisms in active emulsions. *Soft Matt.* 10 (36), 7008–7022.

HOKMABAD, B.V., DEY, R., JALAAL, M., MOHANTY, D., ALMUKAMBETOVA, M., BALDWIN, K.A., LOHSE, D. & MAASS, C.C. 2021 Emergence of bimodal motility in active droplets. *Phys. Rev.* X 11 (1), 011043.

G. Li and D.L. Koch

- HU, W.-F., LIN, T.-S., RAFAI, S. & MISBAH, C. 2019 Chaotic swimming of phoretic particles. *Phys. Rev. Lett.* 123 (23), 238004.
- Hu, J., Zhou, S., Sun, Y., Fang, X. & Wu, L. 2012 Fabrication, properties and applications of janus particles. *Chem. Soc. Rev.* 41 (11), 4356–4378.
- ICHIKAWA, M., TAKABATAKE, F., MIURA, K., IWAKI, T., MAGOME, N. & YOSHIKAWA, K. 2013 Controlling negative and positive photothermal migration of centimeter-sized droplets. *Phys. Rev.* E 88 (1), 012403.
- IZRI, Z., VAN DER LINDEN, M.N., MICHELIN, S. & DAUCHOT, O. 2014 Self-propulsion of pure water droplets by spontaneous Marangoni-stress-driven motion. *Phys. Rev. Lett.* **113** (24), 248302.
- JOHNSON, R.E. & SADHAL, S.S. 1983 Stokes flow past bubbles and drops partially coated with thin films. Part 2. Thin films with internal circulation—a perturbation solution. *J. Fluid Mech.* **132**, 295–318.
- JOHNSON, R.E. & SADHAL, S.S. 1985 Fluid mechanics of compound multiphase drops and bubbles. *Annu. Rev. Fluid Mech.* 17 (1), 289–320.
- Krüger, C., Klös, G., Bahr, C. & Maass, C.C. 2016 Curling liquid crystal microswimmers: a cascade of spontaneous symmetry breaking. *Phys. Rev. Lett.* 117 (4), 048003.
- LAVRENTEVA, O.M., ROSENFELD, L. & NIR, A. 2011 Shape change, engulfment, and breakup of partially engulfed compound drops undergoing thermocapillary migration. *Phys. Rev.* E **84** (5), 056323.
- LI, G. 2022 Swimming dynamics of a self-propelled droplet. J. Fluid Mech. 934, A20.
- LI, J., SINGH, V.V., SATTAYASAMITSATHIT, S., OROZCO, J., KAUFMANN, K., DONG, R., GAO, W., JURADO-SANCHEZ, B., FEDORAK, Y. & WANG, J. 2014 Water-driven micromotors for rapid photocatalytic degradation of biological and chemical warfare agents. ACS Nano 8 (11), 11118–11125.
- MAASS, C.C., KRÜGER, C., HERMINGHAUS, S. & BAHR, C. 2016 Swimming droplets. *Annu. Rev. Condens. Matter Phys.* 7, 171–193.
- MALLORY, S.A., VALERIANI, C. & CACCIUTO, A. 2018 An active approach to colloidal self-assembly. *Annu. Rev. Phys. Chem.* **69**, 59–79.
- MARCHETTI, M.C., JOANNY, J., RAMASWAMY, S., LIVERPOOL, T.B., PROST, J., RAO, M. & SIMHA, R.A. 2013 Hydrodynamics of soft active matter. *Rev. Mod. Phys.* **85** (3), 1143.
- MICHELIN, S. & LAUGA, E. 2014 Phoretic self-propulsion at finite Péclet numbers. J. Fluid Mech. 747, 572–604.
- MICHELIN, S., LAUGA, E. & BARTOLO, D. 2013 Spontaneous autophoretic motion of isotropic particles. *Phys. Fluids* **25** (6), 061701.
- MOFFATT, H.K. 1964 Viscous and resistive eddies near a sharp corner. J. Fluid Mech. 18 (1), 1–18.
- MORI, Y.H. 1978 Configurations of gas-liquid two-phase bubbles in immiscible liquid media. *Intl J. Multiphase Flow* **4** (4), 383–396.
- MOROZOV, M. & MICHELIN, S. 2019a Nonlinear dynamics of a chemically-active drop: from steady to chaotic self-propulsion. *J. Chem. Phys.* **150** (4), 044110.
- MOROZOV, M. & MICHELIN, S. 2019b Orientational instability and spontaneous rotation of active nematic droplets. *Soft Matt.* **15** (39), 7814–7822.
- MOROZOV, M. & MICHELIN, S. 2019c Self-propulsion near the onset of Marangoni instability of deformable active droplets. *J. Fluid Mech.* **860**, 711–738.
- NAGAI, K.H., TAKABATAKE, F., SUMINO, Y., KITAHATA, H., ICHIKAWA, M. & YOSHINAGA, N. 2013 Rotational motion of a droplet induced by interfacial tension. *Phys. Rev.* E **87** (1), 013009.
- NISISAKO, T. 2016 Recent advances in microfluidic production of Janus droplets and particles. *Curr. Opin. Colloid Interface Sci.* 25, 1–12.
- PIMIENTA, V. & ANTOINE, C. 2014 Self-propulsion on liquid surfaces. *Curr. Opin. Colloid Interface Sci.* 19 (4), 290–299.
- ROSENFELD, L., LAVRENTEVA, O.M. & NIR, A. 2008 Thermocapillary motion of hybrid drops. *Phys. Fluids* **20** (7), 072102.
- ROSENFELD, L., LAVRENTEVA, O.M. & NIR, A. 2009 On the thermocapillary motion of partially engulfed compound drops. *J. Fluid Mech.* **626**, 263.
- ROSENFELD, L., LAVRENTEVA, O.M., SPIVAK, R. & NIR, A. 2011 Deformation of a partially engulfed compound drop slowly moving in an immiscible viscous fluid. *Phys. Fluids* 23 (2), 023101.
- RUSHTON, E. & DAVIES, G.A. 1983 Settling of encapsulated droplets at low Reynolds numbers. *Intl J. Multiphase Flow* **9** (3), 337–342.
- RYAZANTSEV, Y.S., VELARDE, M.G., RUBIO, R.G., GUZMÁN, E., ORTEGA, F. & LÓPEZ, P. 2017 Thermo-and soluto-capillarity: passive and active drops. *Adv. Colloid Interface Sci.* **247**, 52–80.
- SADHAL, S.S. & JOHNSON, R.E. 1983 Stokes flow past bubbles and drops partially coated with thin films. Part 1. Stagnant cap of surfactant film–exact solution. *J. Fluid Mech.* **126**, 237–250.

- SCHMITT, M. & STARK, H. 2013 Swimming active droplet: a theoretical analysis. Europhys. Lett. 101 (4), 44008.
- SHANKAR, P.N. 1993 The eddy structure in stokes flow in a cavity. J. Fluid Mech. 250, 371–383.
- SHARDT, O., DERKSEN, J.J. & MITRA, S.K. 2014 Simulations of Janus droplets at equilibrium and in shear. *Phys. Fluids* **26** (1), 012104.
- SHKLYAEV, S., IVANTSOV, A.O., DIAZ-MALDONADO, M. & CORDOVA-FIGUEROA, U.M. 2013 Dynamics of a Janus drop in an external flow. *Phys. Fluids* **25** (8), 082105.
- SINGH, A.V., HOSSEINIDOUST, Z., PARK, B.-W., YASA, O. & SITTI, M. 2017 Microemulsion-based soft bacteria-driven microswimmers for active cargo delivery. ACS Nano 11 (10), 9759–9769.
- SOLER, L., MAGDANZ, V., FOMIN, V.M., SANCHEZ, S. & SCHMIDT, O.G. 2013 Self-propelled micromotors for cleaning polluted water. ACS Nano 7 (11), 9611–9620.
- SUDA, S., SUDA, T., OHMURA, T. & ICHIKAWA, M. 2021 Straight-to-curvilinear motion transition of a swimming droplet caused by the susceptibility to fluctuations. *Phys. Rev. Lett.* **127** (8), 088005.
- SUGA, M., SUDA, S., ICHIKAWA, M. & KIMURA, Y. 2018 Self-propelled motion switching in nematic liquid crystal droplets in aqueous surfactant solutions. *Phys. Rev.* E **97** (6), 062703.
- SUR, S., MASOUD, H. & ROTHSTEIN, J.P. 2019 Translational and rotational motion of disk-shaped Marangoni surfers. *Phys. Fluids* **31** (10), 102101.
- THUTUPALLI, S., SEEMANN, R. & HERMINGHAUS, S. 2011 Swarming behavior of simple model squirmers. New J. Phys. 13 (7), 073021.
- TORZA, S. & MASON, S.G. 1970 Three-phase interactions in shear and electrical fields. *J. Colloid Interface Sci.* 33 (1), 67–83.
- TOYOTA, T., MARU, N., HANCZYC, M.M., IKEGAMI, T. & SUGAWARA, T. 2009 Self-propelled oil droplets consuming 'fuel' surfactant. *J. Am. Chem. Soc.* 131 (14), 5012–5013.
- WALTHER, A. & MULLER, A.H.E. 2013 Janus particles: synthesis, self-assembly, physical properties, and applications. *Chem. Rev.* 113 (7), 5194–5261.
- WANG, X., ZHANG, R., MOZAFFARI, A., DE PABLO, J.J. & ABBOTT, N.L. 2021 Active motion of multiphase oil droplets: emergent dynamics of squirmers with evolving internal structure. *Soft Matt.* 17, 2985–2993.
- WANG, X., ZHOU, Y., KIM, Y., TSUEI, M., YANG, Y., DE PABLO, J.J. & ABBOTT, N.L. 2019 Thermally reconfigurable Janus droplets with nematic liquid crystalline and isotropic perfluorocarbon oil compartments. *Soft Matt.* **15** (12), 2580–2590.
- YOSHINAGA, N. 2014 Spontaneous motion and deformation of a self-propelled droplet. *Phys. Rev.* E **89** (1), 012913.
- YOSHINAGA, N., NAGAI, K.H., SUMINO, Y. & KITAHATA, H. 2012 Drift instability in the motion of a fluid droplet with a chemically reactive surface driven by Marangoni flow. *Phys. Rev.* E **86** (1), 016108.
- ZHANG, J., GRZYBOWSKI, B.A. & GRANICK, S. 2017 Janus particle synthesis, assembly, and application. *Langmuir* **33** (28), 6964–6977.